RECONSTRUCTION OF THE DESCENDING THORACIC AORTA BY MULTIVIEW COMPOUNDING OF 3-D TRANSESOPHAGEAL ECHOCARDIOGRAPHIC AORTIC DATA SETS FOR IMPROVED EXAMINATION AND QUANTIFICATION OF ATHEROMA BURDEN

Maria Chiara Carminati,[*†] Concetta Piazzese,[*‡] Lynn Weinert,[§] Wendy Tsang,[¶] Gloria Tamborini,[†] Mauro Pepi,[†] Roberto Miguel Lang,[§] and Enrico Gianluca Caiani[*]

[*]Department of Electronics, Information and Bioengineering, Politecnico di Milano, Milan, Italy; [†]Centro Cardiologico Monzino, IRCSS, Milan, Italy; [‡]Universitá della Svizzera Italiana, Center for Computational Medicine in Cardiology, Lugano, Switzerland; [§]Noninvasive Cardiac Imaging Laboratories, Department of Cardiology, University of Chicago, Chicago, Illinois, USA; and [¶]Division of Cardiology, University of Toronto, Toronto, Ontario, Canada

(*Received* 1 *July* 2014; *revised* 6 *November* 2014; *in final form* 29 *December* 2014)

INTRODUCTION

Three-dimensional transesophageal echocardiography (3-D TEE) has become one of the most useful imaging modalities for intra-operative management of patients undergoing cardiac surgery (Lang et al. 2006; Vegas and Meineri 2010). At the end of the cardiac examination, TEE is employed to acquire images of the aorta, because of its anatomical proximity when introduced in the esophagus. Indeed, TEE technology allows for the quantification and quantification of aortic lesions, which are known risk factors for complications such as stroke and peripheral embolic events (Hogue et al. 1999; Katsanos et al. 2014). Dimensions and morphology of these aortic lesions have been related to embolic events, and are more prone to occur if lesions are classified as severe or complex plaques, namely, if they are >4 mm thick or contain ulcerations, or mobile elements (Kronzon and Tunick 2006). In particular, characterization and localization of these plaques could be helpful in decreasing neurologic complications, as embolic events can occur after cardiac surgery requiring aortic manipulation. In addition to TEE, other modalities, such as contrast angiography and transthoracic echocardiography (TTE), and more recently epi-aortic ultrasound, magnetic resonance imaging and computed tomography, have been used to image aortic plaques (Bainbridge 2005; Harloff et al. 2012; Kronzon and Tunick 2006; Kutz et al. 1999; Tunick and Kronzon 2000). Among these, 2-D TEE has become the method of choice for visualizing aortic atheromas during cardiac surgery, because of the widespread adoption of intra-operative echocardiography and the ability of TEE to obtain accurate and detailed evaluation of the aorta, as well as plaque composition (Bainbridge 2005; Kronzon

Address correspondence to: Enrico Gianluca Caiani, Department of Electronics, Information and Bioengineering, Politecnico di Milano, Piazza Leonardo da Vinci 32, Milano, Italy. E-mail: enrico.caiani@polimi.it

and Tunick 2006). Nevertheless, 2-D imaging allows analysis only on one cross-sectional plane at a time, thus neglecting the evaluation of true 3-D morphology and the real volumetric extent of atheromas.

Bainbridge (2005) suggested that 3-D TEE, both real time and electrocardiography-gated full volume, could allow a comprehensive evaluation of atheromas in the descending aorta by assessing their thickness, volume and shape. Later, Aggeli et al. (2011) studied the feasibility of using 3-D TEE to depict and quantify the atheromatous burden, and Hammoudi et al. (2014) supported these early findings by comparing 3-D and 2-D technique.

Furthermore, Piazzese et al. (2014) illustrated the feasibility and accuracy of this approach, proposing a semi-automated segmentation of aortic plaques. However, because of the limited field of view, a single 3-D data set can visualize only limited portions of the aorta, and several volumes need to be acquired and analyzed separately to quantify the total amount of plaques and their location at different aortic levels. In this framework, we hypothesized that a compounding strategy could be efficiently designed and implemented to reconstruct wider segments of the descending thoracic aorta, by combining 3-D data sets acquired at different aortic levels.

Accordingly, the aim of the work described here was to propose a robust and efficient framework to reconstruct the descending thoracic aorta by multiview compounding of 3-D TEE aortic data sets to improve visualization and quantification of total atheroma burden. To this end, an *ad hoc* image acquisition protocol to obtain ordered and partially overlapped 3-D TEE aortic data sets was implemented, followed by dedicated image processing to align and fuse all acquired data sets.

Compounding of 3-D echo images has been used previously to improve information content and image quality, with applications mainly in TTE (Gooding et al. 2010; Piella et al. 2013; Rajpoot et al. 2011; Soler et al. 2005; Yao et al. 2011) and in TEE cardiac images (Housden et al. 2013). We present for the first time a compounding approach in which 3-D TEE aortic data sets are combined to allow reconstruction of the descending aorta. In this work, we extend our previous conference paper (Carminati et al. 2014), in which the first step of the proposed approach featuring image registration was presented and applied to a smaller pathologic population.

METHODS

In this section we describe the methodologic framework for reconstruction of the descending thoracic aorta from single-view 3-D TEE aortic data sets. As illustrated schematically in Figure 1, the proposed approach can be summarized in the following stages:

- Image acquisition, performed following an *ad hoc* protocol, designed to acquire spatially ordered and partially overlapping data sets;
- Image registration, in which a rigid pairwise approach is implemented on the basis of the *a priori* knowledge of the acquisition protocol;

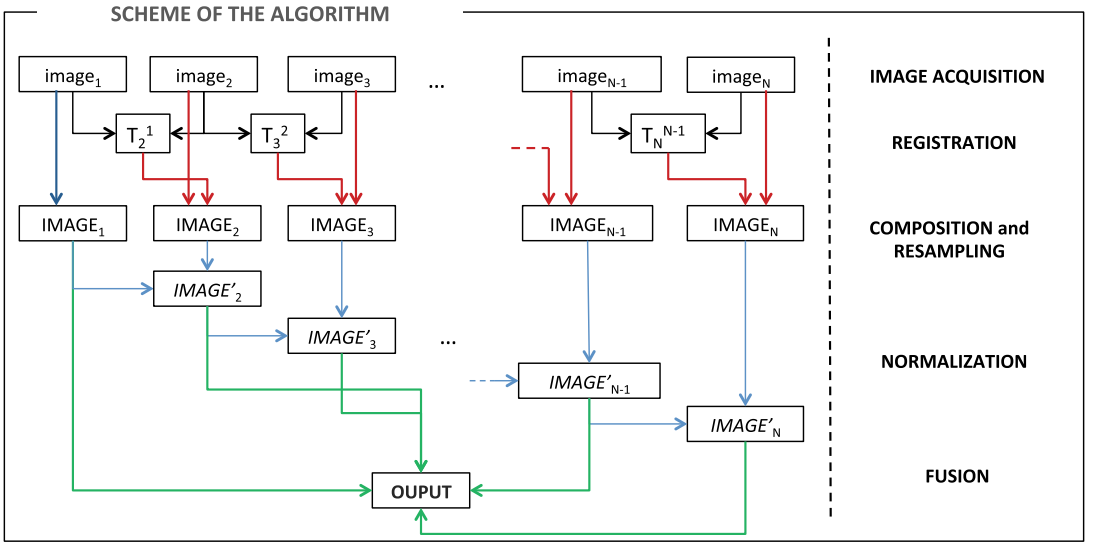

Fig. 1. Framework of the proposed approach: starting from the consecutive overlapped images (image_N), pairwise registration (T_N^{N-1}) was applied, resulting in reciprocally aligned images (IMAGE_N). After their composition and resampling into a common reference system, pairwise normalization (IMAGE'_N) was performed to ensure intensity homogeneity between data sets. Finally, a fusion step was performed.

- Composition, resampling and normalization, aiming at representing all registered and mapped images in the same reference system, with homogeneous intensities;
- Image fusion, performed to obtain a multiview compounded image comprehensive of all acquired single-view 3-D TEE aortic data sets.

Image acquisition protocol

A dedicated acquisition protocol was designed to obtain spatially ordered and partially overlapping 3-D TEE images of the descending thoracic aorta. All the data sets were acquired using ECG-gated real-time 3-D zoom acquisition mode (iE33, X7-2t, Philips, Best, The Netherlands), at 0° with the TEE probe rotated toward the aorta. Sequential overlapping segments were obtained as follows: the first data set was acquired with the probe placed at the deepest esophageal position, adjacent to the diaphragm. The probe was then retracted in approximately 1-cm steps (z-axis, foot-to-head) (Fig. 2), and at each incremental step a new data set was acquired. The distance between the dental incisor and the TEE probe was used to estimate the probe position. This process was repeated until the aortic arch was visualized. To pro-vide consistency in image quality and characteristics be-tween data sets belonging to the same patient, no echo setting was changed during acquisition. Gentle rotation of the probe in different acquisitions was allowed to follow the anatomy of the posterior wall of the descend-ing thoracic aorta.

The benefits of this *ad hoc* protocol are twofold. First, the forced path of the TEE probe along the esophagus ensures spatial order and correspondence between multiple acquisitions; second, the small gap between contiguous probe positions allows large overlap between consecutive volumes, necessary for image matching.

According to this protocol, 17 consecutive patients referred for TEE for a variety of clinical reasons were studied, and partially overlapped 3-D TEE data sets of the descending aorta were acquired. The study was approved by the institutional review board, and each patient gave his or her informed consent. Of the 17 patients, 7 turned out to have aortic plaques. A different number of data sets was acquired for each patient (range: 4–16), according to the anatomical characteristics of the imaged aorta. This variability was due mainly to patient-specific geometry and dimensions of the aorta, as well as to the presence and the extension of aortic plaques. In some cases of clear absence of atherosclerotic disease, a smaller number of consecutive data sets were acquired, in default of clinical interest in performing a larger num-ber of acquisitions.

Typical spatial dimensions for these images were 224 × 224 × 208 voxels with a size of 0.21 × 0.20 × 0.18 mm^3. All data sets were exported in Cartesian converted format (QLab, Philips) for further analysis using custom software.

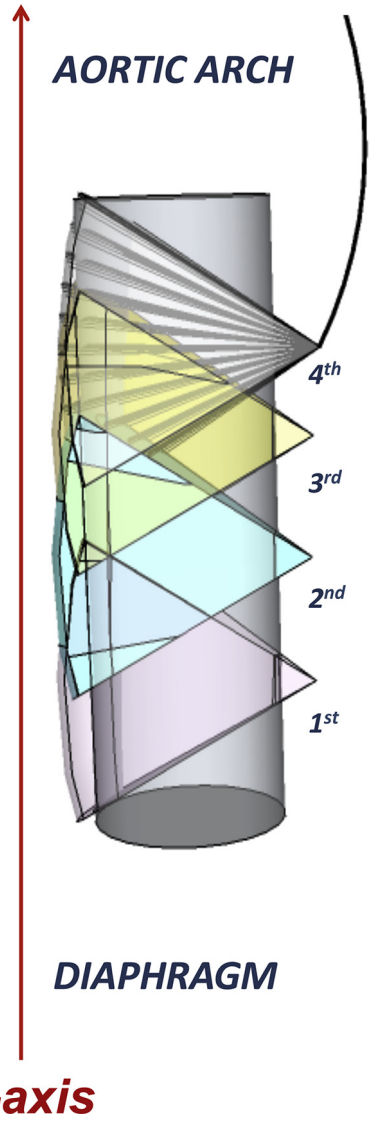

Fig. 2. Schematic of the acquisition protocol, in which sequential overlapping 3-D transesophageal echocardiographic data sets of the descending aorta were acquired.

Registration

The aim of the registration step was to reciprocally align all the acquired data sets from the same patient, bringing them into the same reference system. We exploited the information derived from the acquisition protocol about the reciprocal position and range of overlap between consecutive images as *a priori* knowledge to initialize and guide the registration process. As the information content in the overlapping regions is maximal in adjacent volumes, registration was computed for pairs of contiguous images, and then geometric transformations were composed to map all aligned volumes.

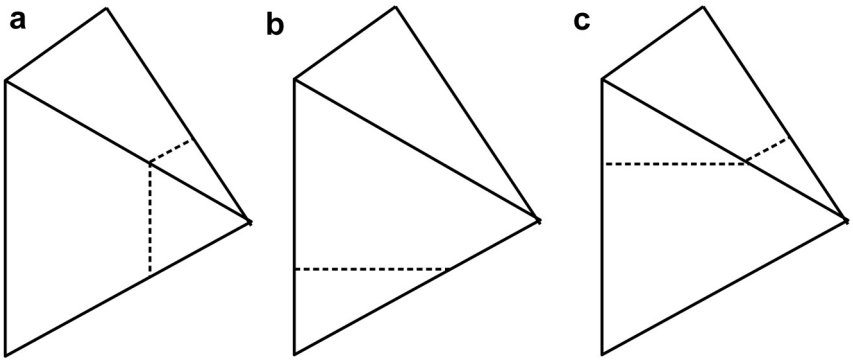

Fig. 3. Mask creation: removal of the tip (a), the bottom (b) or the top portion (c) of the acquisition pyramid to highlight voxels in the data set that are expected to be superimposed for each pair of data sets after registration.

Initialization and mask creation

Because of the lack of frame of reference in echo im-ages and the extremely limited presence of anatomic landmarks in the aortic data sets, the definition of an appropriate initial transformation plays a crucial role in the success of the registration process.

The initialization procedure was automated and relied on the creation of image masks obtained from the original data sets. First, each pyramid-shaped 3-D echo volume included in the cubic image data set was thresholded to obtain a binary image, with white voxels inside the pyramid and black voxels outside. From it, a subvolume was obtained by masking the voxels corresponding to the tip of the pyramid, empirically defined as one-fourth along the pyramid height of the total volume of the bounding box (Fig. 3a). Then, voxels belonging to the upper or lower portion of the binary image, corresponding to one-third of the total volume of the pyramid, according to the reciprocal position of the two data sets to be registered, were set to zero. Namely, for the volume in the considered pair relevant to the deepest esophageal position, the lower subvolume was set to zero, and vice versa (Fig. 3b, c). In this way, the so-obtained masks highlight the voxels in the original data sets that are expected to be superimposed by registration, in agreement with the acquisition protocol.

Their role was twofold: (i) an adequate and automatic transformation to be used to initialize the registration process was obtained by overlying their center of mass; (ii) they were used as masks in the registration to select the voxels to be included in the metric computation. This was necessary because the TEE aortic data sets are characterized by very limited morphologic distinctive features between different data sets. In our experiments we found that, without masking, registration very likely resulted in local optima in which pyramidal shapes are overlapping, particularly for those cases characterized by limited presence of aortic lesions.

Pairwise registration and composition

After the initialization procedure, a standard voxel-based multiresolution algorithm was used to register contiguous pairs of TEE aortic data sets, using the open source ITK library (Ibanez et al. 2003). A 3-D rigid registration approach ($T = \{T_x, T_y, T_z, \Theta_x, \Theta_y, \Theta_z\}$) with three levels of multiresolution and gradient descent optimizer was adopted, and normalized cross-correlation (NCC) between masked images was set as a similarity metric to guide the registration process. The three-level multiresolution was obtained with isotropic downsampling factors of 4, 2 and 1. Maximum and minimum step lengths were set to 1.00 and 0.01 for the first level of multiresolution, with downsampling factors of 10 and 4, respectively. Customarily, the fixed and moving images were set as the one obtained at the deepest esophageal position and the consecutive data set, respectively, according to the temporal order of image acquisition.

Temporal correspondence between data sets was ensured by always selecting the first frame, corresponding to ECG-triggered end diastole, for use in the analysis. We assumed that a rigid transformation was adequate to align our data sets, as temporal correspondence was ensured by ECG gating, and acquisition parameters were kept fixed during the entire TEE exam.

After registration was calculated for all image pairs, transformations were composed to bring all data sets into the same reference system. We considered as the reference image the first volume acquired according to the study protocol, that is, the data set corresponding to the deepest esophageal position. Then, all transformations were mapped with respect to the first image, according to the equation

$$T_1^n = \prod_{i=1}^{n} T_i^{i+1} \tag{1}$$

where T_1^n is the transformation of the nth image with respect to the position of the first acquired image. The

entire algorithm was developed in C++ using the Insight Toolkit (Ibanez et al. 2003).

Validation on simulated data

In two patients (P_1 and P_2), two single 3-D TEE images, with isotropic spatial resolutions respectively of 0.17 and 0.25 mm, were used to obtain two pairs of data sets each to test the performance of the pairwise registration algorithm. Both P_1 and P_2 were characterized by atherosclerotic disease: in P_1, well-defined aortic pla-ques were present, whereas slight thickening was observed for P_2. These characteristics were chosen to test the algorithm's efficiency in different pathologic con-ditions. Simulated data to be used in the validation were obtained by extracting two subvolumes (volume of inter-est 1, VOI_1, and volume of interest 2, VOI_2) from each 3-D TEE image P_1 and P_2 by cutting 30% of the upper or lower portion of the original volume along the z-axis, respectively, to obtain partially overlapped volumes with known ground truth positions.

For both P_1 and P_2, VOI_1 was set as reference image whereas VOI_2 was artificially misaligned. Known roto-translations were applied by randomly sampling a linear distribution of translation values in the range -10; $+10$ mm along the z-direction and -5; $+5$ mm along the x and y directions and of rotation values in the range of -10°, $+10^\circ$ along each axis. Translation along the z-axis was greater than that along the x- and y-axes to simulate the esophageal position of the probe, in agreement with the acquisition protocol.

With this scheme, 30 different transformations were obtained and applied to each VOI_2, which was resampled along the corresponding VOI_1 grid. Then, each subvolume was processed to compensate for the presence of speckle noise, to prevent the same pattern in the two VOIs belonging to the same original data set from influ-encing registration performance. First, 3-D homomorphic filtering was applied to reduce the presence of the original speckle pattern. Briefly, it consisted of the application of a logarithmic transform on the original image, followed by low-pass filtering in the Fourier domain (Gaussian smoothing filter, $\sigma = 1.5$). Finally, filtered images were contaminated by adding independent realizations of multiplicative noise (gamma distribution, $\sigma = 0.1$), to simulate an uncorrelated noisy "speckle-like" condition in images to be registered.

Registration of the pairs of data sets was performed as previously described, and residual errors after registration were computed. Mono- and multiresolution approaches were tested on the two phantom images P_1 and P_2, and their performances compared in terms of residual error and computational time. Overall, 120 pairwise registrations were computed.

Clinical validation

Several criteria were considered to quantify the pairwise registration accuracy in contiguous data sets in the studied population.

Custom software for semi-automated segmentation of aortic plaques requiring minimal user interaction was applied to obtain a 3-D mesh from each data set in which the posterior aortic wall and atheromas were identified. Briefly, the 3-D mesh of the aortic lumen, including both aortic wall and plaques, was obtained by automated thresholding and by applying the marching cubes algorithm to the binary volume. Threshold value was chosen empirically and set equal to 175. Segmentation of aortic wall and plaques was then performed by locally fitting the aortic wall cross section with an elliptic curve defined starting from manual initialization in a limited number of axial projections within the volume (please refer to Piazzese et al. [2014] for more details).

For each pair of contiguous data sets, the geometric transformation computed from registration was applied to the corresponding 3-D meshes to allow for a first visual assessment of correspondence between detected plaques (Fig. 4). Furthermore, quantitative assessment of the registration was performed by computing mean surface distance (MSD) and Hausdorff distance (HD) between 3-D meshes of the same represented plaque in contiguous data sets. Finally, displacements along the acquisition z-axis between all consecutive data sets after registration was chosen as a measure of consistency with the probe displacement defined in the acquisition protocol.

Image fusion

The fusion process results in a single reconstructed image including all main information from the volumes belonging to the same patient. To this effect, we implemented specific pre-processing steps and investigated the application of four different algorithms based on voxel intensities, quantitatively assessing their ability to improve image quality.

Volume of interest extraction, resampling and pairwise normalization

Before fusion of aortic TEE data sets, pre-processing is necessary to ensure good image quality of the final image. First, a VOI was manually defined for all single-view images. This procedure allows removal of the tip of the pyramidal data set and the ends of each aortic segment, to preserve only the significant informative content for each single volume. In fact, the tip of the pyramid is representative only of some limited parts of the anterior wall of the aorta and, if included in the fusion process, would result in a partial and discontinuous reconstruction. Furthermore, the basal section of the pyramidal data set is prone to be affected by noise

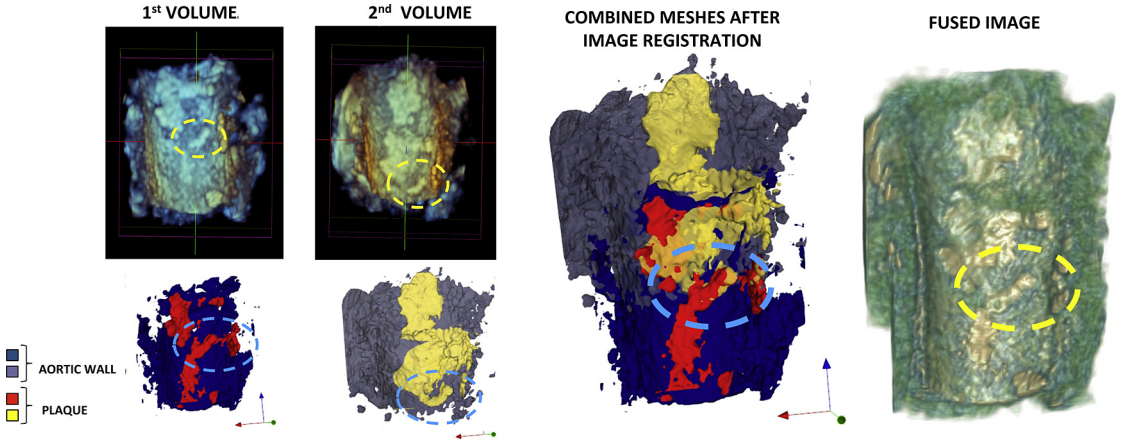

Fig. 4. Example of the clinical validation procedure. Top left: Two contiguous 3-D transesophageal echocardiographic data sets in which a detail of the same plaque is highlighted with a *yellow circle*. Bottom left: Corresponding result, as 3-D mesh, of plaque segmentation obtained with custom software, with a detail of the same plaque highlighted with a *blue circle*. Right: Result of the image registration, defined using the original 3-D transesophageal echocardiographic data, applied to the 3-D meshes and correspondent combined volume rendering. The overlap of the two corresponding plaque details is highlighted.

depending on the relative position and orientation between the probe and the posterior aortic wall. For these reasons, these portions are excluded from the VOIs before obtaining the compounded image. In our protocol, the VOI selection for each data set was applied as part of the image segmentation procedure performed to validate the registration algorithm, as described earlier, and therefore, it was not repeated for image fusion.

All registered and cropped images of the same patient were transformed and resampled to fill the same Cartesian array in the 3-D space. The dimensions of this array were computed by taking into account the image boundaries of all data sets after registration and composition, whereas the spatial resolution was set equal to the resolution of the original image with smaller voxel size. Voxels outside the single-view images were set to zero in the resampling process.

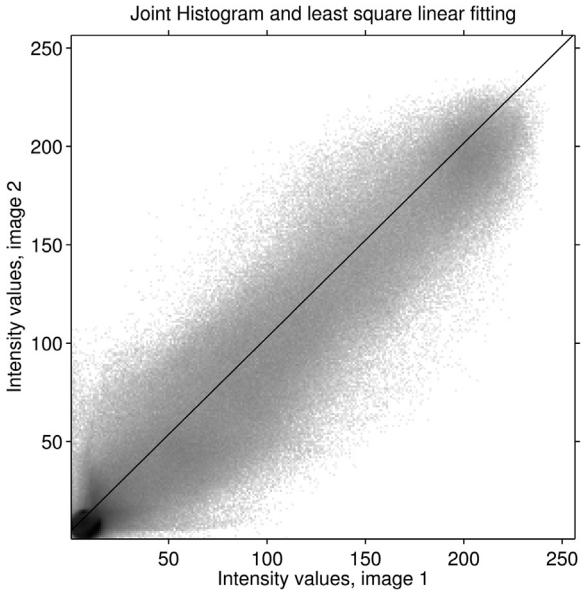

Fig. 5. Example of joint histogram of voxel intensities between two adjacent data sets after registration. Least-squares linear fitting approximates linear relationship between intensities.

Finally, normalization of voxel intensities was implemented. In fact, there can be differences in the intensity of the same tissue region visible in different image scans because of the interposing structures crossed by the ultrasound pressure waveform, with possible impact on the quality of the compounded image (Yao et al. 2011). In Yao et al. (2011), automated intensity normali-zation, based on the calculation of the joint histogram of all images with respect to the first acquired image set as reference, was proposed to solve this problem. Least-squares fitting was then applied to each histogram to compute best-fit lines. The line with the median slope was finally selected and used to normalize the intensity of all images with respect to the reference one.

In this study, we implemented a similar approach, in which normalization followed a pairwise scheme. Namely, the first couple of adjacent and resampled volumes, IMAGE_1 and IMAGE_2, was considered for joint-histogram and best-fit line computation (Fig. 5). Intensity values of IMAGE_2 were consequently linearly mapped and normalized with respect to IMAGE_1. Then, similarly, IMAGE_3 was normalized after joint histogram computation with normalized IMAGE_2 with least-squares line fitting. The process was iterated until all data sets belonging to the same acquisition protocol were processed. For the computation of linear regression by

least-squares fitting, we adopted the QT algorithm implemented in the Template Numerical Toolkit (http://math.nist.gov/tnt/).

Intensity-based image fusion and quality indices

After resampling and normalization, the following image fusion strategies were investigated and compared: (i) maximum, (ii) mean, (iii) geometric mean and (iv) wavelet based. The first three methods are based on the combination of the overlapping subvolumes following the voxel-by-voxel mathematical rules:

$$I_{\max} = \max\{I_1, I_2, \ldots, I_n\}$$
$$I_{\text{mean}} = \frac{1}{N}\sum_{i=1}^{N} I_i, \text{ where } I_i \neq 0 \quad (2)$$
$$I_{\text{geom\_mean}} = \sqrt[n]{\sum_{i=1}^{N} I_i}, \text{ where } I_i \neq 0$$

Here, I_i is the ith image that contributes to the computation of the compounded images $I_{\max}$, I_{mean} and $I_{\text{geom\_mean}}$, and N is the number of images considered for each patient.

Details in single-view echo images, such as aortic wall and plaques, are characterized by high intensity values and, therefore, are expected to be transferred to the fused image when applying the maximum intensity fusion rule. However, according to this scheme, image ar-tifacts and noise could also be preserved in the final im-age, possibly reducing signal-to-noise ratio (SNR). This approach was previously used for ultrasound image fusion in Leotta and Martin (1999), Rajpoot et al.(2011) and Yao et al. (2011).

Conversely, fusion rules based on mean calculation are expected to reduce noise and artifacts at the expense of contrast of the output image. With the aim of image compounding, several authors have tested mean (Behar et al. 2003; Rajpoot et al. 2011; Yao et al. 2011) and geometric mean (Behar et al. 2003) fusion rules. In our study, voxels that were set to zero by the resampling pre-processing were not taken into account in computation of the mean fusion rules, as pointed out by eqn (2).

The wavelet-based fusion approach was first proposed by Soler et al. (2006) for compounding 3-D breast ultrasound images and then by Rajpoot et al. (2011) for multiview fusion of real-time 3-D TTE, with promising results in terms of both contrast and SNR. As in Rajpoot et al. (2011), we implemented a one-level for-ward wavelet transform for each volume, thus obtaining one low-frequency and seven high-frequency wavelet coefficients. Then, maximum and mean fusion rules were respectively applied on low-frequency and high-frequency coefficients. Finally, an inverse wavelet transform was applied to obtain the final compounded image. In our experiments, we used a quadrature mirror filter using biorthogonal 3.5 kernel for wavelet decomposition, adapting the code derived from the Generalized Image Fusion Toolkit (Mueller 2006).

Quantitative and comparative assessment of the fusion methods was performed by computing several quality indices of the fused image (Rajpoot et al. 2011; Soler et al. 2005): percentage difference in contrast (ΔC), contrast-to-noise ratio (ΔCNR) and signal-to-noise ratio (ΔSNR). To this aim, we segmented all fused images following the semi-automatic approach described under Clinical Validation (Piazzese et al. 2014), and im-age voxels were accordingly classified as belonging to the blood pool, the aortic wall or atheromas. Quality indices were computed twice, considering separately the differences between the blood pool and the aortic wall and the aortic wall and atheromas. Furthermore, percentage change in field-of-view (ΔFOV) was calculated to quantify the increase in the image bounds in the compounded images caused by the geometry of the acquisition, independently of the fusion approach. In our experiments, ΔFOV was specifically dependent on the number of consecutive data sets that was possible to obtain by the specifications of the acquisition protocol. Further details of each of these indices can be found in the Appendix.

RESULTS

Image registration

Residual registration errors after simulations on the two artificially misaligned images (P_1 and P_2) are summa-rized in Table 1. Limited errors were found in both mono-and multiresolution approaches, with median values of the order of the pixel resolution in the residual misalign-ments along the axis direction (ΔT_z). No significant dif-ferences were found in registration performance (mono vs. multi, $p < 0.05$, Kruskal–Wallis test). Instead, compu-tational times varied significantly, resulting in mean values of 737 and 293 s for mono- and multiresolution, respectively. These results illustrated the feasibility and accuracy of the applied strategy in registering pairs of consecutive and partially overlapped data sets. The sig-nificant decrease in computational time supported the choice to adopt the multiresolution approach for image registration on clinical data sets.

For the 17 consecutive patients, 170 3-D TEE data sets were acquired and 153 pairwise registrations consequently computed. All pairs of registered data sets were visually checked by an experienced observer, as described under Clinical Validation, and 90.2% (138/153) were judged reliable for correspondence of aortic wall and atheromas, when present. The remaining 9.8% of cases (15/153), in which the registration did not lead

Table 1. Residual registration error in the two phantom data sets (P_1 and P_2) expressed as delta translations (ΔT_x, ΔT_y, ΔT_z) and rotations ($\Delta\Theta_x$, $\Delta\Theta_y$, $\Delta\Theta_z$)

	P_1		P_2	
Applied roto-translation	Mono	Multi	Mono	Multi
ΔT_x (mm)	−0.018 (−0.048, 0.0009)*	−0.018 (−0.059, −0.0005)	−0.011 (−0.26, 0.034)	−0.014 (−0.034, 0.030)
ΔT_y (mm)	−0.0009 (−0.023, 0.115)	0.011 (−0.023, 0.144)	0.063 (−0.019, 0.314)	0.053 (−0.029, 0.244)
ΔT_z (mm)	−0.098 (−0.235, 0.0004)	−0.104 (−0.224, 0.004)	−0.112 (−0.473, 0.049)	−0.117 (−0.438, 0.066)
$\Delta\Theta_x$ (°)	0.032 (0.0006, 0.080)	0.037 (0.013, 0.095)	0.039 (−0.028, 0.061)	0.0513 (−0.0068, 0.0755)
$\Delta\Theta_y$ (°)	0.037 (−0.047, 0.281)	0.054 (−0.017, 0.318)	0.116 (−0.029, 0.474)	0.132 (−0.035, 0.385)
$\Delta\Theta_z$ (°)	−0.009 (−0.037, 0.021)	−0.014 (−0.038, 0.006)	0.017 (−0.013, 0.028)	0.019 (−0.002, 0.034)

* Median (25th; 75th percentile).

to satisfactory results, were excluded from the following image fusion process. In particular, of the 15 failed pairwise registrations, 6 belonged to the same patient, for whom 11 consecutive data sets in total acquired. For this patient, successful aortic reconstruction was per-formed using only five consecutive volumes. The remain-ing failure cases belonged to different patients, and the relevant volumes were excluded from the reconstruction. In case the excluded data set was at the extremities of the acquisition chain (*i.e.*, first or last acquired pyramidal vol-ume), very few disadvantages were found in the final reconstruction because of the large amount of overlap of consecutive volumes (with a loss of approximately 1 cm, in accordance with the acquisition protocol). In case the failed registration corresponded to the *i*th data set located in the middle of the acquisition chain, the registration was re-computed between the $(i-1)$th and $(i+1)$th data sets, resulting in success. Again, this was possible because of the large overlap between data sets.

An example of registration failure is illustrated in Figure 6, where the rigid transformation computed by the registration was not able to properly match the aortic wall of the two consecutive data sets.

Translation along the z-axis imposed by the registration was found equal to 6.52 (2.38; 10.85) mm (median and interquartile range), in the range of the manual probe displacement between data sets defined in the acquisition protocol. In the subset of seven patients characterized by the presence of aortic plaques, a total of 57 3-D TEE data sets were overall acquired and 50 pairwise registrations computed. Among these, 31 pairs of volumes presented at least one corresponding plaque. In these cases, MSD and HD were computed between pairs of surfaces representing the same plaque in contiguous data sets, resulting in median (interquartile) values of 1.11 (0.66; 3.15) mm and 5.6 (3.4; 8.27) mm, respectively.

Differences in image quality and field-of-view may, however, result in slightly different segmentation of corresponding plaques in consecutive data sets, thus influencing the computation of MSD and HD. This can be observed in Figure 4, where the same plaque is correctly overlapped after registration, but represented differently in the two data sets. To evaluate this effect on the quantification of registration performance, distance indices were re-computed taking into account the amount of overlap between surfaces caused mainly by the registration performance, according to the following criterion. Corresponding surface plaques were cropped according to the intersections of the bounding boxes of the two original surfaces along the x-axis (left−right direction) and z-axis (long axis of the vessel). Instead, the dimensions along the y-axis (anterior−posterior direction) were preserved, as representative of the goodness of the overlap after registration. The evaluation of MSD and HD on these cropped regions resulted in median (interquartile) values of 0.55 (0.34; 0.92) and 3.4 (2.5; 5.1) mm, respectively, significantly smaller compared with the first results.

The composition of all registered data sets in the same reference system was finally checked by an experienced observer, who visually analyzed the results by means of volume as well as surface rendering of the compounded volumes. No clinically significant distortions were reported.

Image fusion

The fusion step was performed after pairwise registration and normalization, by applying all four methods previously presented. However, for three patients in whom 9, 10 and 12 consecutive data sets were consequently acquired, an extremely high computational burden was required to compute the wavelet-based fusion method. To overcome this limitation, prior to wavelet fusion, downsampling of the data sets was required, using a step of 1.5 for the first two patients and a step of 2 for the last one.

As expected, there was a considerable increase in the FOV as a result of image fusion (278% [162%; 326%]). Figure 7 highlights this finding, visualizing an example of compounding results with respect to a single-view

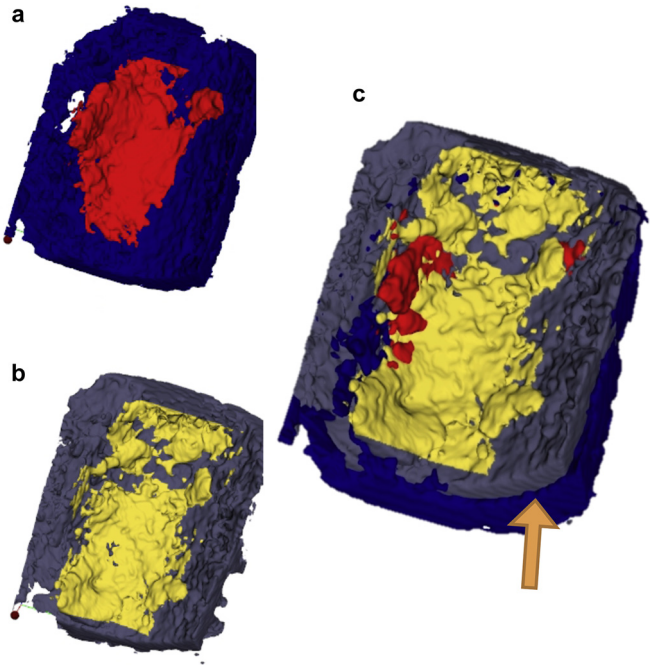

Fig. 6. Example of registration failure: (a, b) pairs of data sets to be registered, (c) data set position after registration. The algorithm failed at matching aortic walls, and no clear overlap between corresponding plaques was noticeable.

image. Also, the 2-D orthogonal cut-planes obtained from 3-D volumes are shown for each of the four fusion methods. The most noticeable improvement can be appreciated in the sagittal projection of multiview images, in which the increase in the extension of the imaged aorta is visible compared with the original single-view data set. Tables 2 and 3 summarized the results of the computed fusion quality indices (ΔC, ΔCNR and ΔSNR), when considering voxels belonging to aortic lumen and blood pool, or belonging to the aortic wall and atheromas, computed for all patients and for those patients characterized by the presence of aortic plaques, respectively. In the first case, all fusion techniques resulted in increased C, CNR and SNR. The Kruskal–Wallis statistics was applied to compare their performance: a reduced ΔC for the wavelet-based approach with respect to max, mean and geometric mean fusion rules was found, whereas a larger ΔCNR for the wavelet-based approach than for mean fusion rule was observed. When considering voxels belonging separately to the aortic wall and atheromas (Table 3), C and CNR were found to be mainly decreased, whereas SNR was increased for all the approaches considered, with no significant differences.

DISCUSSION

Identification and characterization of aortic lesions are recognized as clinically relevant, as the presence of aortic plaques is an independent risk factor for stroke and peripheral embolization (Cohen et al. 1997) and is also associated with carotid, coronary and renal artery disease (Fazio et al. 1993; Kronzon and Tunick 2006). TEE technology is a suitable tool for assessing aortic atherosclerosis (Vaduganathan et al. 1997; Vegas and Meineri 2010), as it is routinely performed to identify cardiac sources of emboli and, during cardiac surgery, to guide the introduction of the cannula into the aorta to prevent peri-procedural plaque embolization.

We propose a robust and efficient approach to the 3-D reconstruction of the descending thoracic aorta by fusion of single-view 3-D TEE aortic data sets. Recent develop-ments in medical image fusion research have been leading to promising results, with potential useful impact on clinical applications such as diagnosis, monitoring and analysis (James and Dasarathy 2014). In particular, com-pounding of multiple echo images was previously pro-posed, with a reported valuable improvement in image quality (Behar et al. 2003; Gooding et al. 2010; Krücker et al. 2000; Leotta and Martin 1999; Piella et al. 2013; Rajpoot et al. 2011; Soler et al. 2005, 2006; Yao et al. 2011). Among these, compounding strategies have been proposed and tested in phantoms (Behar et al. 2003), using 3D TTE (Piella et al. 2013; Rajpoot et al. 2011; Soler et al. 2005; Yao et al. 2011) and 3-D fetal cardiac images (Gooding et al. 2010), 3-D breast images (Krücker et al. 2000; Soler et al. 2006) and shoulder rotator cuff 3-D images (Leotta and Martin 1999).

To the best of our knowledge, this study describes for the first time a strategy for the registration and fusion

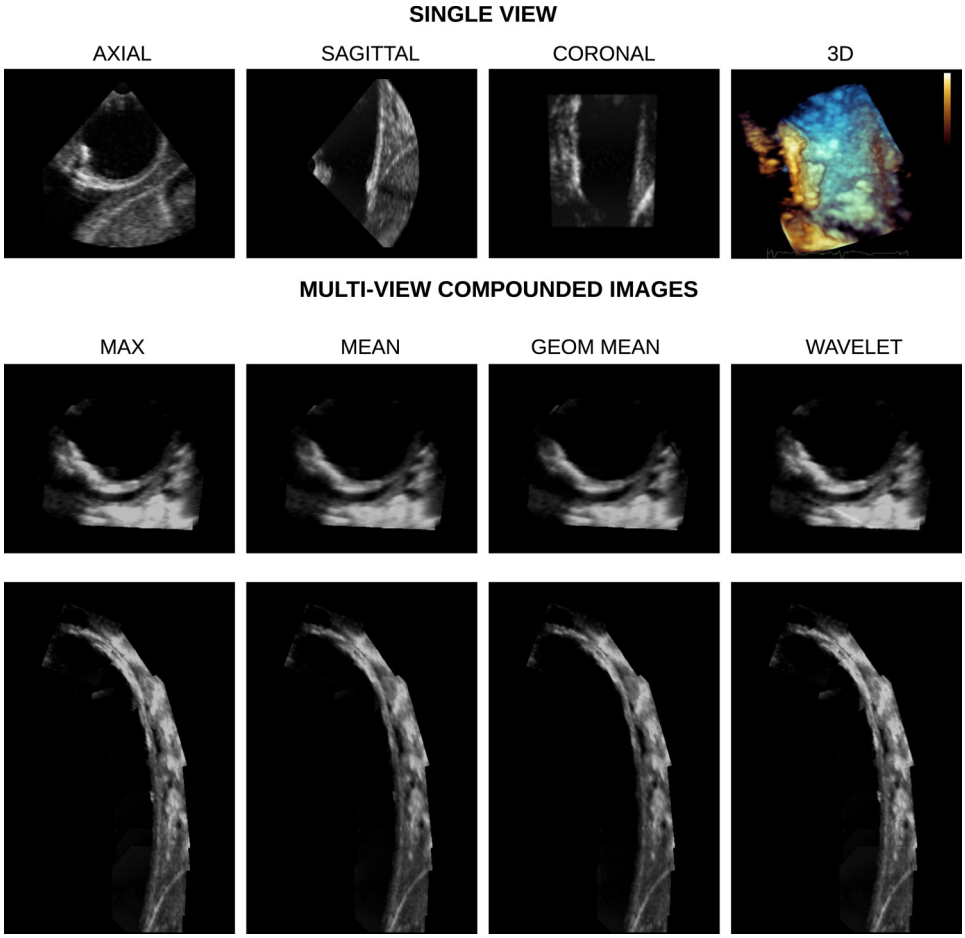

Fig. 7. Original (top) and compounded 3-D echo images using the four fusion algorithms investigated (bottom). Two-dimensional orthogonal cut-planes from 3-D images are presented. Multiview image fusion allows for the morphologic reconstruction of the descending aorta and the increase in field-of-view is particularly noticeable in the sagittal projection of multiview images compared with single-view data set.

of 3-D TEE contiguous aortic data sets. Our method allows for the 3-D morphologic reconstruction of the descending aorta, by augmenting the field-of-view of 3-D TEE aortic data sets, thus potentially enabling precise spatial localization of atherosclerotic plaques and quantification of plaque burden in the reconstructed segment. Other potential diagnostic applications of our methodology include the study of patients with aortic chronic diseases who can benefit from an extended visualization of the thoracic aorta, whereas this analysis is precluded in patients affected by acute aortic syndromes with unstable hemodynamics (aortic atherosclerosis plus atheromas, aortic penetrating ulcers, pseudo-aneurysm or aneurysm).

Our study is based on a dedicated acquisition protocol that slightly differs from routine 3-D TEE aortic examination. However, the complexity of the proposed protocol is minimal and potentially applicable in all patients undergoing a TEE examination.

Table 2. Quality indices for aortic lumen versus blood pool

Quality indices	Max	Mean	Geometric mean	Wavelet
ΔC (%)	30.7 (18.8; 36.6)*†	16.89 (14.05; 21.47)†	19.9 (15.48; 22.97)†	13.1 (−9.77; 7.34)
ΔCNR (%)	17.95 (6.05; 28.54)	20.07 (6.2; 25.93)†	14.23 (8.26; 27.42)	34.28 (19.3; 55.05)
ΔSNR (%)	52.96 (46.10; 74.76)	53.24 (35.79; 68.68)	68.56 (53.24; 87.68)	60.13 (34.53; 160.98)

CNR = contrast-to-noise ratio; SNR = signal-to-noise ratio.
* Median (25th; 75th percentile).
† $p < 0.05$ versus wavelet, Kruskal–Wallis test.

Table 3. Quality indices for aortic wall versus atheromas

Quality indices	Max	Mean	Geometric mean	Wavelet
ΔC (%)	−17.35 (−42.15; 5.9)*	5.55 (−35.5; 9.94)	−3.02 (−40.34; 2.59)	−40.11 (−55.47; −18.88)
ΔCNR (%)	−28.64 (−47.27; −9.45)	−1.9 (−46.10; 20.19)	−17.37 (−47.21; 10.62)	−21.32 (−52.72; 4.55)
ΔSNR (%)	11.04 (−3.87; 37.73)	16.28 (−2.32; 58.40)	19.94 (−1.9; 59.54)	16.76 (8.9; 76.28)

CNR = contrast-to-noise ratio; SNR = signal-to-noise ratio.
* Median (25th; 75th percentile).

Compared with previous studies, in which rigid registration represented the first step for multiview fusion of cardiac real-time 3-D TTE (Rajpoot et al. 2011; Soler et al. 2005; Yao et al. 2011) or TEE (Housden et al. 2013) images, registration of 3-D TEE aortic data sets represents a more difficult task, because of the lack of characteristic structures and anatomic landmarks. To cope with these limits, we specifically designed an image acquisition protocol resulting in sequentially ordered and partially overlapped data sets. In this way, the *a priori* knowledge of pairwise data set position was used to perform automatic and robust initialization necessary for image registration. The proposed registration step was based on the well-known intensity-based multireso-lution approach and guided by the NCC metric. As a result of artificially introduced misalignment in the pairs of data sets derived from a single 3-D TEE acquisition, residual registration errors were limited, proving the robustness of this approach.

On individual data sets, each pairwise registration was initially checked by visual inspection, resulting in a success rate >90%. Failure in the remaining 10% could be explained by artifacts and deformations caused by the ECG gating acquisition or breathing motion, where affine or non-rigid registration should be considered. In 7 of 17 patients in whom plaques were present, quantita-tive validation based on computation of MSD and HD indices indicated that corresponding atheromas in contig-uous volumes were correctly overlapped after registra-tion, thus supporting the feasibility and accuracy of the proposed method in keeping the clinical information relevant to plaque presence. It is worth noting that the reported higher HD values are justified by the fact that maximum distances between surfaces is increased as plaques located on overlapping areas could also extend to non-overlapping regions. In addition, the displacement along the z-axis resulting from the registration process between contiguous data sets was consistent with what was expected from the probe displacement in the acquisition protocol.

Three-dimensional morphologic reconstruction of the descending thoracic aorta was finally achieved by fusion of registered, mapped and normalized single-view data sets. The most noticeable improvement of our compounding approach is the increase in FOV of the fused image with respect to the original acquisitions, which is related to the geometry of the acquisition and the number of consecutive acquired data sets, independently of the fusion technique.

Comparison of the four different fusion approaches implemented indicated that all investigated methods succeeded in improving contrast and suppressing noise, when considering separately aortic lumen and blood pool. However, in contrast to previous studies (Gooding et al. 2010; Rajpoot et al. 2011; Soler et al. 2005; Yao et al. 2011), for this specific application we did not find a unique method that was able to override the others based on the computed performance metrics. Of note, no significant differences between mean, geometric mean and maximum approaches were found, whereas the wavelet approach proved to be the least effective in improving contrast and the highest in computational burden, thus requiring downsampling before fusion in 3 of 17 patients (17%).

Quality indices were also computed by considering separately aortic wall and atheromas. This was possible with the use of custom software allowing 3-D plaque segmentation (Piazzese et al. 2014), so that quality indices were computed from all information included in the 3-D volumes. In this case, all adopted techniques succeeded in improving SNR, but failed in enhancing contrast and CNR, probably because the echogenicity of plaques is variable and dependent on calcific content (Cohen et al. 1997; Kronzon and Tunick 2006). Therefore, higher contrast between aortic wall and atheromas is expected only for calcific plaques.

Our work has some limitations. First, the absence of a true gold standard could have affected our results relevant to performance of the algorithm. However, computed indices on both artificially misaligned and paired data sets showed little residual errors and distances between recognized structures. Furthermore, qualitative analysis of the compounded data sets excluded the presence of clinically significant distortions for all of the populations studied, thus illustrating the good registration and fusion performance. Moreover, as pilot validation with a potential gold standard technique, in one patient who underwent transcatheter aortic valve implantation, a computed tomography scan (GE Medical System, 512 × 512 × 626 voxels with spacing

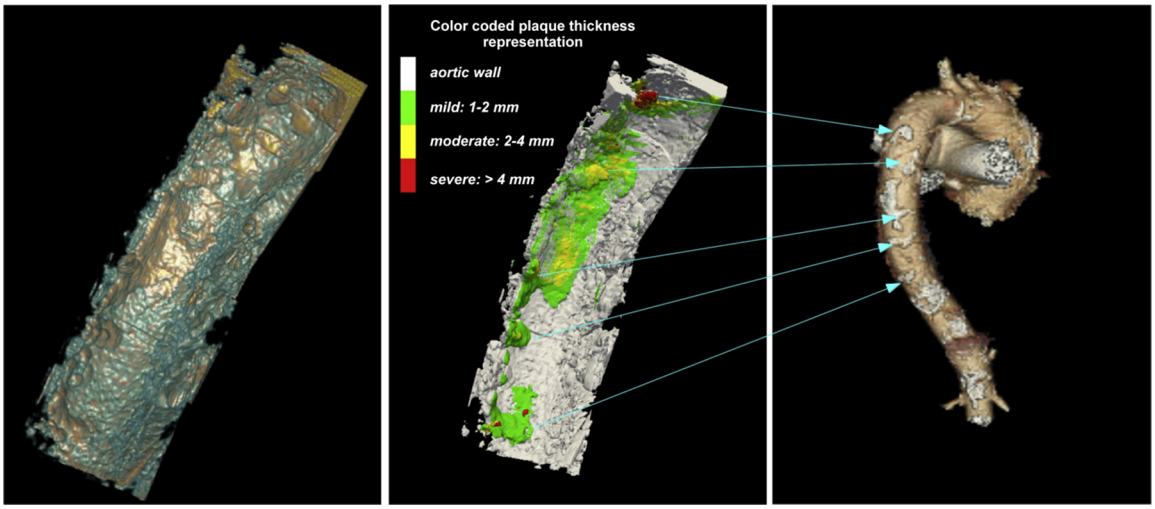

Fig. 8. Left: Volume rendering of the 3-D transesophageal echocardiographic fused image. Center: Surface rendering after segmentation of the fused image with color-coded plaque thickness. Right: Volume rendering of the reconstructed aorta from computed tomography. Plaque correspondence between 3-D compounded echo and computed tomography is highlighted by *blue arrows*.

$0.48 \times 0.48 \times 0.88$ mm) was also available. We used the volume rendering of these images for an additional visual comparison with the compounded 3-D TEE, by carefully comparing plaque morphology on the posterior aortic wall visible in both echo and CT. As depicted in Figure 8, there was visual correspondence between pla-que position and morphology, thus confirming the feasi-bility of the proposed registration and fusion approach to obtain a single view of the descending aorta and its pla-que burden for clinical purposes.

Also, we examined a limited number of patients, particularly those (7 patients) with atheromas in the descending aorta. As the specific imaging protocol was applied to consecutive patients, we were not able to discriminate between positive and negative cases relative to inclusion criteria. Moreover, we also wanted to test our algorithm in the absence of clear plaques. In future studies, a preliminary evaluation could be performed before image acquisition, including only patients with plaques who could benefit from application of the proposed methodology.

An additional limitation is that the reconstruction was possible for the posterior wall of the descending aorta from the diaphragmatic level up to the distal aortic arch, whereas the anterior wall had to be excluded because of the intrinsic limitations of TEE acquisitions (Dávila-Román et al. 1996). Limited parts of the aortic arch that may be imaged could be included in the reconstruction whether their acquisition fulfills the protocol criteria, that is, adjacency and partial overlap with the previously acquired data sets. Improved display of the reconstructed posterior descending aortic wall can be further achieved by both volume rendering and surface rendering after seg-mentation, thus allowing quantitative evaluation of the atherosclerotic disease of the aorta (Piazzese et al. 2014). Other imaging modalities, such as CT and MRI, potentially allow more comprehensive evaluation of the entire aorta (Bainbridge 2005; Fayad et al. 2000; Harloff et al. 2012; Kronzon and Tunick 2006), but with the limitation of requiring longer acquisition times, general contraindications higher costs and the use of ionizing radiation and contrast agents. Furthermore, the quantitative analysis of the geometry and pathology of the aorta over an extended field-of-view might be clinically valuable in the case where the TEE probe is already in place, as in the intra-operative management of patients with aortic disease.

CONCLUSIONS

Three-dimensional TEE contiguous and partially overlapped data sets of the descending thoracic aorta can be efficiently compounded with a novel approach based on a dedicated acquisition protocol and custom software constituted by pairwise registration based on *a priori* knowledge and image fusion. Our study represents the first attempt at 3-D morphologic reconstruction of the descending aorta, investigating the use of 3-D TEE, with promising potential application in quantification of the extension and relative position of aortic atheromas.

REFERENCES

Aggeli C, Kazazaki C, Felekos I, Roussakis G, Lagoudakou S, Skoumas J, Toutouzas K, Tousoulis D, Pitsavos C, Stefanadis C.

Role of real time-3D transesophageal echocardiography in evaluating the atheromatous burden of thoracic aorta in patients with heterozygous familial hypercholesterolemia: Comparison with 2D transesophageal study. Int J Cardiol 2011;150:92–93.
Bainbridge D. 3-D imaging for aortic plaque assessment. Semin Cardiothorac Vasc Anesth 2005;9:163–165.
Behar V, Adam D, Friedman Z. A new method of spatial compounding imaging. Ultrasonics 2003;41:377–384.
Carminati M, Piazzese C, Weinert L, Tsang W, Tamborini G, Pepi M, Lang R, Caiani E. Automated registration of 3D TEE datasets of the descending aorta for improved examination and quantification of atheromas burden. In: . Berlin/Heidelberg: Springer; 2014. p. 83–92.
Cohen A, Tzourio C, Bertrand B, Chauvel C, Bousser MG, Amarenco P, on behalf of the FAPS Investigators. Aortic plaque morphology and vascular events: A follow-up study in patients with ischemic stroke. Circulation 1997;96:3838–3841.
Dávila-Román V, Phillips K, Daily B, Dávila R, Kouchoukos N, Barzilai B. Intraoperative transesophageal echocardiography and epiaortic ultrasound for assessment of atherosclerosis of the thoracic aorta. J Am Coll Cardiol 1996;28:942–947.
Fayad Z, Nahar T, Fallon J, Goldman M, Aguinaldo J, Badimon J, Shinnar M, Chesebro J, Fuster V. In vivo magnetic resonance evaluation of atherosclerotic plaques in the human thoracic aorta: A comparison with transesophageal echocardiography. Circulation 2000;101:2503–2509.
Fazio G, Redberg R, Winslow T, Schiller N. Transesophageal echocardiographically detected atherosclerotic aortic plaque is a marker for coronary artery disease. J Am Coll Cardiol 1993;21:144–150. Gooding M, Rajpoot K, Mitchell S, Chamberlain P, Kennedy S, Noble J. Investigation into the fusion of multiple 4-D fetal echocardiography images to improve image quality. Ultrasound Med Biol 2010;36:957–966.
Hammoudi N, Ihaddaden M, Lang S, Laveau F, Ederhy S, Michel PL, Alamowitch S, Cohen A. Three-dimensional transesophageal echocardiography for descending aortic atheroma: A preliminary study. Int J Cardiovasc Imaging 2014;30:1529–1537.
Harloff A, Brendecke S, Simon J, Assefa D, Wallis W, Helbing T, Weber J, Frydrychowicz A, Vach W, Weiller C, Markl M. 3D MRI provides improved visualization and detection of aortic arch plaques compared to transesophageal echocardiography. J Magn Reson Im-aging 2012;36:604–611.
Hogue C, Murphy S, Schechtman K, Dávila-Román V. Risk factors for early or delayed stroke after cardiac surgery. Circulation 1999;100:642–647.
Housden R, Ma YL, Arujuna A, Nijhof N, Cathier P, Gijsbers G, Bullens R, Gill J, Rinaldi C, Parish V, Rhode K. Extended-field-of-view three-dimensional transesophageal echocardiography using image-based x-ray probe tracking. Ultrasound Med Biol 2013;39:993–1005.
Ibanez L, Schroeder W, Ng L, Cates J. The ITK Software Guide. Clifton Park, NY: Kitware, Inc. Available at: http://www.itk.org/ItkSoftwareGuide.pdf; 2003. Accessed February 5, 2015.
James A, Dasarathy B. Medical image fusion: A survey of the state of the art. Inform Fusion 2014;19:4–19.
Katsanos A, Giannopoulos S, Kosmidou M, Voumvourakis K, Parissis J, Kyritsis A, Tsivgoulis G. Complex atheromatous plaques in the de-scending aorta and the risk of stroke: A systematic review and meta-analysis. Stroke 2014;45:1764–1770.
Kronzon I, Tunick P. Aortic atherosclerotic disease and stroke. Circulation 2006;114:63–75.
Krücker J, Meyer C, LeCarpentier G, Fowlkes J, Carson P. 3D spatial compounding of ultrasound images using image-based nonrigid registration. Ultrasound Med Biol 2000;26:1475–1488.
Kutz S, Lee V, Tunick P, Krinsky G, Kronzon I. Atheromas of the thoracic aorta: A comparison of transesophageal echocardiography and breath-hold gadolinium-enhanced 3-dimensional magnetic resonance angiography. J Am Soc Echocardiogr 1999;12:853–858.
Lang R, Mor-Avi V, Sugeng L, Nieman P, Sahn D. Three-dimensional echocardiography the benefits of the additional dimension. J Am Coll Cardiol 2006;48:2053–2069.
Leotta D, Martin R. Three-dimensional spatial compounding of ultrasound scans with incidence angle weighting. IEEE Ultrason Symp 1999;2:1605–1608.
Mueller D. The generalised image fusion toolkit (GIFT). 2006. Available at: http://hdl.handle.net/1926/216. Accessed February 5, 2015.
Piazzese C, Tsang W, Sotaquira M, Kronzon I, Lang R, Caiani E. Semi-automated detection and quantification of aortic plaques from three-dimensional transesophageal echocardiography. J Am Soc Echocardiogr 2014;27:758–766.
Piella G, De Craene M, Butakoff C, Grau V, Yao C, Nedjati-Gilani S, Penney G, Frangi A. Multiview diffeomorphic registration: Application to motion and strain estimation from 3D echocardiography. Med Image Anal 2013;17:348–364.
Rajpoot K, Grau V, Noble J, Szmigielski C, Becher H. Multiview fusion 3-D echocardiography: Improving the information and quality of real-time 3-D echocardiography. Ultrasound Med Biol 2011;37:1056–1072.
Soler P, Delso G, Villain N, Angelini E, Bloch I. Superresolution spatial compounding techniques with application to 3D breast ultrasound imaging. In: Emilianov S, Walker WF, eds. Proc SPIE 2006;6147. Proceedings, Medical Imaging 2006: Ultrasonic Imaging and Signal Processing.
Soler P, Gerard O, Allain P, Saloux E, Angelini E, Bloch I. Comparison of fusion techniques for 3D+T echocardiography acquisitions from different acoustic windows. Comput Cardiol 2005;2005:141–144.
Tunick P, Kronzon I. Atheromas of the thoracic aorta: Clinical and therapeutic update. J Am Coll Cardiol 2000;35:545–554. Vaduganathan P, Ewton A, Nagueh S, Weilbaecher D, Safi H, Zoghbi W. Pathologic correlates of aortic plaques, thrombi and mobile "aortic debris" imaged in vivo with transesophageal echocardiography. J Am Coll Cardiol 1997;30:357–363.
Vegas A, Meineri M. Three-dimensional transesophageal echocardiography is a major advance for intra-operative clinical management of patients undergoing cardiac surgery: A core review. Anesth Analg 2010;110.
Yao C, Simpson J, Schaeffter T, Penney G. Multi-view 3D echocardiography compounding based on feature consistency. Phys Med Biol 2011;56:6109.

APPENDIX: QUALITY INDICES

Percentage variation in contrast caused by image fusion is defined as

$$\Delta C_{\mathrm{AW-BP}} = \left[\frac{\mu^{f}_{\mathrm{AW}} - \mu^{\mathrm{f}}_{\mathrm{BP}}}{\frac{1}{N}\sum_{i=1}^{N}\left(\mu^{i}_{\mathrm{AW}} - \mu^{i}_{\mathrm{BP}}\right)} - 1\right] * 100$$
$$\Delta C_{\mathrm{AW-ATH}} = \left[\frac{\mu^{f}_{\mathrm{AW}} - \mu^{f}_{\mathrm{ATH}}}{\frac{1}{N}\sum_{i=1}^{N}\left(\mu^{i}_{\mathrm{AW}} - \mu^{i}_{\mathrm{ATH}}\right)} - 1\right] * 100 \quad \text{(A.1)}$$

where μ_{AW}, μ_{BP}, μ_{ATH} are the mean intensity values of the aortic wall (AW), blood pool (BP) and atheromas (ATH), respectively; N is the total number of source single-view images, and f and i represent the fused and ith data sets, respectively.

Percentage variation in contrast-to-noise ratio caused by image fusion is defined as

$$\Delta\mathrm{CNR}_{\mathrm{AW-BP}} = \left[\frac{\mathrm{CNR}^{\mathrm{f}}_{\mathrm{AW-BP}}}{\frac{1}{N}\sum_{i=1}^{N}\mathrm{CNR}^{i}_{\mathrm{AW-BP}}} - 1\right] * 100$$
$$\Delta\mathrm{CNR}_{\mathrm{AW-ATH}} = \left[\frac{\mathrm{CNR}^{\mathrm{f}}_{\mathrm{AW-ATH}}}{\frac{1}{N}\sum_{i=1}^{N}\mathrm{CNR}^{i}_{\mathrm{AW-ATH}}} - 1\right] * 100 \tag{A.2}$$

where CNRs of the fused or single-view images are computed as

$$\mathrm{CNR}_{\mathrm{AW-BP}} = \frac{\mu_{\mathrm{AW}} - \mu_{\mathrm{BP}}}{\sqrt{(\sigma_{\mathrm{AW}})^2 + (\sigma_{\mathrm{BP}})^2}}$$
$$\mathrm{CNR}_{\mathrm{AW-ATH}} = \frac{\mu_{\mathrm{AW}} - \mu_{\mathrm{ATH}}}{\sqrt{(\sigma_{\mathrm{AW}})^2 + (\sigma_{\mathrm{ATH}})^2}} \tag{A.3}$$

and σ is the standard deviation of intensity values in the specified region.

Percentage variation in signal-to-noise ratio due to image fusion is defined as

$$\Delta\mathrm{SNR}_{\mathrm{AW-BP}} = \frac{\Delta\mathrm{SNR}_{\mathrm{AW}} - \Delta\mathrm{SNR}_{\mathrm{BP}}}{2}$$
$$\Delta\mathrm{SNR}_{\mathrm{AW-ATH}} = \frac{\Delta\mathrm{SNR}_{\mathrm{AW}} - \Delta\mathrm{SNR}_{\mathrm{ATH}}}{2} \tag{A.4}$$

where $\Delta\mathrm{SNR}_x$, relative to the xth region, is defined as

$$\Delta\mathrm{SNR}_x = \left[\frac{\mu^{\mathrm{f}}_x / \sigma^{\mathrm{f}}_x}{\frac{1}{N}\sum_{i=1}^{N}\mu^{i}_x / \sigma^{i}_x} - 1\right] * 100 \tag{A.5}$$

Percentage change in field-of-view (ΔFOV) caused by image fusion is defined as

$$\Delta\mathrm{FOV} = \left[\frac{\mathrm{FOV}_{\mathrm{f}}}{\frac{1}{N}\sum_{i=1}^{N}\mathrm{FOV}_i} - 1\right] * 100$$
$$\mathrm{FOV} = \Sigma_{v=1}^{n} d(v), \quad \text{where } d(v) = \begin{cases} 1 \text{ foreground} \\ 0 \text{ background} \end{cases} \tag{A.6}$$

where v represents the vth voxel in the image, n is the total number of voxels in each image and foreground and background are considered regions inside and outside the image pyramid, respectively. ΔFOV allows us to quantify the increase in image boundaries in the compounded images caused by the geometry of the acquisition, independently of the fusion approach. In our experiments, ΔFOV was specifically dependent on the number of consecutive data sets that were possible to acquire in accordance with the specifications of the acquisition protocol.